



Numerical simulations on the flow past a flexible filament with two fixed ends at a low Reynolds number

Huanyu Zhang¹, Yakun Zhao¹, Peng Wang^{1,2}, Binrong Wen^{1,2}, Xinliang Tian^{1,2} 
and Hao Liu^{3,4} 

¹State Key Laboratory of Ocean Engineering, School of Ocean and Civil Engineering, Shanghai Jiao Tong University, Shanghai 200240, PR China

²SJTU Sanya Yazhou Bay Institute of Deep Sea Sci-Tech, Sanya 572000, PR China

³Shanghai Jiao Tong University and Chiba University International Cooperative Research Center (SJTU-CU ICRC), Shanghai Jiao Tong University, Shanghai 200240, PR China

⁴Graduate School of Engineering, Chiba University, Chiba 263-8522, Japan

Corresponding author: Xinliang Tian, tianxinliang@sjtu.edu.cn

(Received 22 June 2024; revised 6 January 2025; accepted 5 February 2025)

This study explores an interesting fluid–structure interaction scenario: the flow past a flexible filament fixed at two ends. The dynamic performance of the filament under various inclination angles (θ) was numerically investigated using the immersed boundary method. The motion of the filament in the θ – Lr space was categorised into three flapping modes and two stationary modes, where Lr is the ratio of filament length to the distance between its two ends. The flow fields for each mode and their transitions were introduced. A more in-depth analysis was carried out for flapping at a large angle (FLA mode), which is widely present in the θ – Lr space. The maximum width W of the time-averaged shape of the filament has been shown to strongly correlate with the flapping frequency. After non-dimensionalising based on W , the flapping frequency shows little variation across different Lr and θ . Moreover, two types of lift variation process were also identified. Finally, the total lift, drag and lift-to-drag ratio of the system were studied. Short filaments, such as those with $Lr \leq 1.5$, were shown to significantly increase lift and the lift-to-drag ratio over a wide range of θ compared with a rigid plate. Flow field analysis concluded that the increases in pressure difference on both sides of the filament, along with the upper part of the flexible filament having a normal direction closer to the y direction, were the primary reasons for the increase in lift and lift-to-drag ratio. This study can provide some guidance for the potential applications of flexible structures.

Key words: flow–structure interactions

1. Introduction

The motion of flexible bodies in fluid flows is a widespread phenomenon in nature. For example, fish obtain thrust for swimming forwards through active bending of their bodies (Huber 2000; Triantafyllou, Triantafyllou & Yue 2000; Müller 2003), trees and aquatic plants passively alter their shapes in wind or water to reduce drag (Alben, Shelley & Zhang 2002; Gosselin *et al.* 2010; Zhang, He & Zhang 2020), and flags flap in the wind. All these natural phenomena can be simplified into the motion of one or more flexible bodies in fluid flows, which, despite their structural simplicity, contain complex dynamics, including thrust generation, drag reduction and self-excited oscillations. Inspired by these natural scenarios, extensive research has been conducted to explore the underlying mechanical principles governing the motion of flexible bodies in fluid flows. As a relatively fundamental model, the motion of three-dimensional (3-D) flags or simplified two-dimensional (2-D) filaments in a uniform inflow has received extensive attention. Zhang *et al.* (2000) conducted soap film experiments to simulate the motion of a filament with its head fixed in a 2-D flow field, discovering two motion states related to the filament length: the stretched-straight state and the oscillatory state. Subsequently, as shown in figure 1(a), numerical simulations for a single head-fixed filament immersed in a flow field were conducted, where the effects of filament length, inflow velocity, bending coefficient and the mass ratio between the filament and fluid on the flapping of the filament were extensively studied (Zhu & Peskin 2002; Farnell, David & Barton 2004; Connell & Yue 2007; Huang, Shin & Sung 2007; Alben & Shelley 2008; Michelin, Smith & Glover 2008). Notably, compared with Zhang *et al.* (2000), a new chaotic mode was discovered (Connell & Yue 2007; Alben & Shelley 2008; Michelin *et al.* 2008). Numerous numerical simulations also indicated that higher inflow velocities, smaller bending coefficients and larger mass ratios are more conducive to the filament entering the flapping state.

In the above scenarios, a common feature of the flexible filaments is that their heads are fixed while their tails are free. In addition to the basic study on the motion modes, the applications of this model has also been investigated, especially in energy capture (Tang, Païdoussis & Jiang 2009; Michelin & Doaré 2013). Apart from this most basic installation method, figure 1(b,c) illustrates two other methods for flexible filaments or plates corresponding to different boundary conditions, both of which have also been extensively studied in terms of fundamental research and related applications. The first is where the head of the filament is free and the tail is clamped, forming an inverted flag. Inverted flags with different lengths and bending coefficients also exhibit different motion modes including straight stationary mode, flapping mode and chaotic mode through interaction with fluids like the head-fixed filament (Kim *et al.* 2013; Gurugubelli & Jaiman 2015; Sader *et al.* 2016; Yu, Liu & Chen 2017). The second installation method is to clamp both edges of the filament. The filament under this kind of boundary condition can exploit fluid forces from the surrounding fluid to exhibit unique snap-through (Kim *et al.* 2021; Mao, Liu & Sung 2023). Due to the lower self-excitation speeds of the two models shown in figure 1(b,c), related applied research has also explored the use of the motion of flexible structures for energy harvesting (Orrego *et al.* 2017; Kim *et al.* 2020; Bai *et al.* 2022; Mazharmanesh *et al.* 2022). The device based on the model in figure 1(c) has been designed to capture fluid energy in wind and waves (Kim *et al.* 2020; Bai *et al.* 2022).

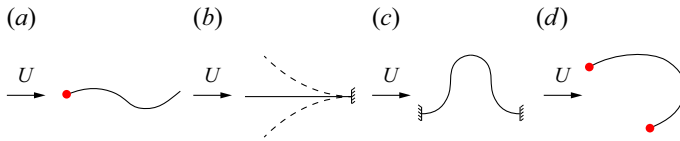


Figure 1. Four fluid–structure interaction models involving a flexible filament: (a) the head is fixed by the simply supported condition, while the tail is free; (b) the head is free, while the tail is clamped; (c) both the head and tail are clamped; (d) both head and tail are fixed by the simply supported condition.

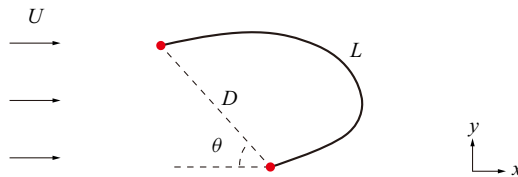


Figure 2. Schematic diagram of a flexible filament with two fixed ends under different inclination angles (θ).

Apart from the three filament installation scenarios corresponding to different boundary conditions mentioned above, there is another basic scenario where the filament is fixed in a uniform inflow at both ends through the simply supported condition, as shown in figure 1(d). The impact of this new boundary condition on fluid–structure interactions remains unknown. Investigating this interaction can provide insights into the motion modes of filaments and potentially contribute to applications involving flexible structures, such as enhancing dynamic performance and optimising energy harvesting. In addition, many common scenarios in nature that involve rich dynamic mechanisms, such as parachutes, paragliders and hot air balloons in the air, as well as fixed banners in the wind, are related to this simplified model. Although the model in figure 1(d) is a simplification of a finite-span thin plate in the real world, this fundamental model has not yet been extensively studied. Therefore, this paper will investigate the motion of a filament fixed by simply supported boundary conditions in a uniform flow, where the bending stiffness of the filament is very small to minimise its impact. Since the filament length and inflow angle have significant influence on the filament motion, for instance, at an inflow angle close to zero, shorter filaments may oscillate up and down between the two fixed points under the action of fluid, while too long filaments may extend a long tail past the downstream fixed point. Additionally, when the filament length is small and the inflow angle is appropriate, the filament is similar to a 3-D membrane wing (Song *et al.* 2008; Waldman & Breuer 2017; Tzezana & Breuer 2019; He & Wang 2020; Mathai *et al.* 2022), which could be beneficial for enhancing dynamic performance. Therefore, the inflow angle and the length of the filament are the main parameters studied in this paper.

The remainder of this paper is structured as follows. Section 2 details the computational framework, encompassing the physical model, numerical approach and validation of the code. Following this, in § 3, we discuss the findings from our numerical results. Finally, the conclusions are presented in § 4.

2. Computational model

2.1. Problem definition

Figure 2 illustrates the fluid–structure interaction (FSI) system studied in this paper, which consists of a single filament fixed at both ends by the simply supported conditions.

Here, L and D represent the length of the filament and the distance between the endpoints of the filament, respectively. In this context, D is used as the characteristic length to non-dimensionalise L , yielding the length ratio $Lr = L/D$. The system is placed in a uniform inflow parallel to the x -axis, with an inflow velocity of U . The angle of the inflow is denoted by the acute angle formed between the line connecting the endpoints of the filament and the x -axis, also referred to as the inclination angle (θ) of the structure. In fact, the model of a one-dimensional (1-D) filament placed in a 2-D flow field is a simplification of the model where a spanwise infinite membrane is placed in a 3-D flow field.

In this system, the 2-D incompressible viscous flow is governed by the dimensionless Navier–Stokes (N-S) equations as follows:

$$\frac{\partial \mathbf{u}}{\partial t} + \mathbf{u} \cdot \nabla \mathbf{u} = -\nabla p + \frac{1}{Re} \nabla^2 \mathbf{u} + \mathbf{f}, \tag{2.1}$$

$$\nabla \cdot \mathbf{u} = 0, \tag{2.2}$$

where $\mathbf{u} = (u, v)$, t , p and Re denote the velocity vector, time, pressure and Reynolds number, respectively. Here, \mathbf{f} denotes the Eulerian momentum force acting on the adjacent fluid, used to maintain the no-slip condition along the immersed boundary (IB). Additionally, \mathbf{u} , t , p and \mathbf{f} are non-dimensionalised by U , D/U , $\rho_0 U^2$ and $\rho_0 U^2/D$, respectively, where ρ_0 is the fluid density. The Reynolds number is defined as $Re = \rho_0 U D / \mu$, with μ representing the fluid dynamic viscosity.

The deformation and motion of the flexible filament are described using Lagrangian variables and are expressed as

$$\frac{\partial^2 \mathbf{X}}{\partial t^2} = \frac{\partial}{\partial s} \left(T \frac{\partial \mathbf{X}}{\partial s} \right) - \frac{\partial^2}{\partial s^2} \left(\gamma \frac{\partial^2 \mathbf{X}}{\partial s^2} \right) - \mathbf{F}, \tag{2.3}$$

$$\frac{\partial \mathbf{X}}{\partial s} \cdot \frac{\partial \mathbf{X}}{\partial s} = 1, \tag{2.4}$$

where s represents the Lagrangian coordinate along the filament. Here, $\mathbf{X}(s, t)$ denotes the Eulerian position of a Lagrangian point s at time t . Additionally, T is the tension force along the filament and γ is the bending coefficient defined as $\gamma = EI$, where EI is the bending rigidity of the filament (Huang *et al.* 2007; Ye *et al.* 2017); \mathbf{F} signifies the Lagrangian momentum force exerted on the flexible filament by the surrounding fluid. The inextensibility condition is satisfied by introducing (2.4). Using (2.3) and (2.4), a Poisson equation for calculating the tension force T can be derived (Huang *et al.* 2007). Equations (2.3) and (2.4) have been non-dimensionalised by introducing the following characteristic scales: $\rho_1 U^2/D$ for \mathbf{F} , $\rho_1 U^2$ for T and $\rho_1 U^2 D^2$ for γ , where ρ_1 denotes the line density difference between the filament and the surrounding fluid. The present dimensionless approach has been widely used in many previous studies (Uhlmann 2005; Yu 2005; Huang *et al.* 2007; Ye *et al.* 2017; Mao *et al.* 2022).

At the two fixed ends, the simply supported boundary conditions are applied

$$\mathbf{X}|_{s=0} = \mathbf{X}_0, \quad \frac{\partial^2 \mathbf{X}}{\partial s^2} \Big|_{s=0} = (0, 0), \tag{2.5}$$

$$\mathbf{X}|_{s=Lr} = \mathbf{X}_{Lr}, \quad \frac{\partial^2 \mathbf{X}}{\partial s^2} \Big|_{s=Lr} = (0, 0), \tag{2.6}$$

where \mathbf{X}_0 and \mathbf{X}_{Lr} represent the coordinates of the two fixed ends of the filament within the Eulerian coordinate system.

2.2. Numerical methods

In this study, the immersed boundary method (IBM) is employed to describe the interaction between the fluid and the structure, which has been extensively adopted for simulating similar scenarios (Peskin 2002; Mao *et al.* 2022). The Lagrangian force \mathbf{F} can be calculated by the feedback law (Goldstein, Handler & Sirovich 1993; Huang *et al.* 2007; Mao *et al.* 2021; Sun *et al.* 2022)

$$\mathbf{F}(s, t) = \alpha \int_0^t (\mathbf{U}_{ib}(s, t) - \mathbf{U}(s, t)) dt' + \beta (\mathbf{U}_{ib}(s, t) - \mathbf{U}(s, t)), \quad (2.7)$$

where α and β are large negative constants (Huang *et al.* 2007; Ye *et al.* 2017), with $\beta = \alpha \Delta t$ used to eliminate one free constant, β (Huang & Sung 2009). The velocity of the filament, $\mathbf{U}(s, t)$, is expressed by $\mathbf{U}(s, t) = d\mathbf{X}(s, t)/dt$. The fluid velocity at the IB, \mathbf{U}_{ib} , is obtained by interpolation at the IB using the surrounding fluid velocity

$$\mathbf{U}_{ib}(s, t) = \int_{\Omega} \mathbf{u}(\mathbf{x}, t) \delta(\mathbf{X}(s, t) - \mathbf{x}) d\mathbf{x}. \quad (2.8)$$

The Dirac delta function δ is employed to facilitate the transformation between Eulerian and Lagrangian variables (Peskin 2002). In this way, the Eulerian momentum force \mathbf{f} can also be calculated by spreading the Lagrangian momentum force \mathbf{F} to the surrounding Eulerian grids,

$$\mathbf{f}(\mathbf{x}, t) = \rho \int_{\Gamma} \mathbf{F}(s, t) \delta(\mathbf{x} - \mathbf{X}(s, t)) ds, \quad (2.9)$$

where $\rho = \rho_1/(\rho_0 D)$ is the result of non-dimensionalisation and Γ denotes the structure domain.

The computational framework for the entire FSI system consists of three components. The fluid motion part is implemented based on the finite volume method (FVM), with modifications made to the icoFOAM fluid solver within OpenFOAM-8. The filament motion is resolved through the finite difference method (FDM), with spatial discretisation in the Lagrangian coordinate. The fluid–structure interaction component is developed based on (2.7), (2.8) and (2.9). A detailed description of the discretisation and solution of the filament motion equations and the IBM equations can be found from Huang *et al.* (2007). During the solver development process, we make modifications based on the icoFOAM solver. First, we add the Eulerian momentum force \mathbf{f} , as shown in (2.1), into the process of solving the N-S equations in icoFOAM solver. Furthermore, we incorporated the structural solver algorithm and the fluid–structure coupling algorithm into our fluid solver file. The calculation process is shown as follows.

- (i) At the n th time step, we know the fluid velocity field \mathbf{u}^n and the filament positions \mathbf{X}^n and \mathbf{X}^{n-1} . Then we can calculate the Lagrangian momentum force \mathbf{F}^n by (2.7).
- (ii) Update the position of the filament to obtain \mathbf{X}^{n+1} by (2.3).
- (iii) Spread the Lagrangian momentum force \mathbf{F}^n to get the Eulerian momentum force \mathbf{f}^n using Equation (2.9). Solve N-S equations to update the fluid velocity field and pressure field.

In this study, a multi-block Cartesian mesh strategy is employed to reduce computing costs. The mesh around the IB is sufficiently fine to meet the requirements for high computational accuracy. The boundary condition of the computational domain is set as follows: a uniform velocity profile ($u = U, v = 0$) is specified at the inlet, symmetry boundary conditions ($\frac{\partial u}{\partial y} = 0, v = 0$) are applied at the top and bottom boundaries,

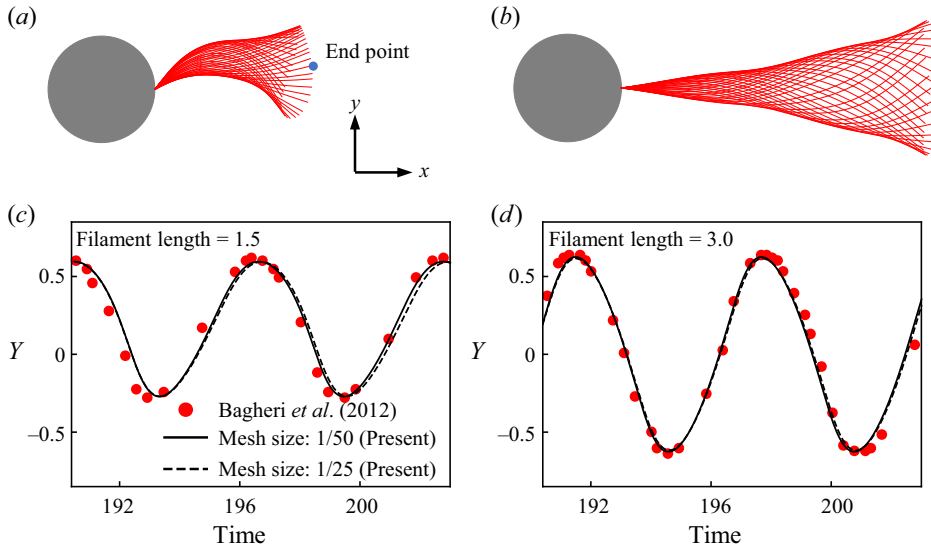


Figure 3. (a,b) Schematic diagram of the system including a circular cylinder and an attached filament with lengths of 1.5 and 3. (c,d) Position of the end point of the filament in the y direction.

while zero gradient conditions ($\frac{\partial u}{\partial x} = 0$, $\frac{\partial v}{\partial x} = 0$) are imposed at the outlet. Subsequently, some models containing flexible filaments will be simulated to validate our code.

2.3. Validation

We first simulated the flow past a circular cylinder with a single attached filament, as depicted in figure 3(a,b). The simply supported boundary condition was employed at the attachment point of the filament. The diameter of the circular cylinder was dimensionless and set to 1, with the dimensionless lengths of the filament being 1.5 and 3, respectively. For other critical parameters, such as filament mass and bending coefficient, we referred entirely to Bagheri, Mazzino & Bottaro (2012). However, it should be noted that the non-dimensionalisation process of our method is different from that of Bagheri *et al.* (2012), where the fluid density was used to non-dimensionalise the bending coefficient. The filament positions at different times are illustrated in figure 3(a,b). Additionally, figure 3(c,d) displays the varying positions of the endpoints of two filaments in the y direction over time, using two different fluid grid sizes Δx . Our results show good agreement with the work of Bagheri *et al.* (2012).

To further validate our numerical method, we simulated the flow over a flexible filament clamped at two edges, as shown in the inset of figure 4(a). The filament was placed along the flow direction, with the distance between its two fixed endpoints being D , and the filament length was L . This paper simulated the movement of two filaments of different lengths and monitored the midpoint trajectories in both the x and y directions. The parameters for the two filaments were $D/L = 0.5$, $\gamma = 0.02$ and $D/L = 0.589$, $\gamma = 0.005$, respectively. The midpoint positions of the filaments from our simulation results are shown in figure 4(a,b), exhibiting a high level of consistency with the results obtained by Mao *et al.* (2023). The results indicate that our solver has good accuracy in solving the motion of a single filament in a uniform flow.

Furthermore, some numerical trials were conducted to determine the key computational parameters for subsequent formal calculations, including the size of the computational domain, the minimum grid size Δx of the computational domain, the time step Δt

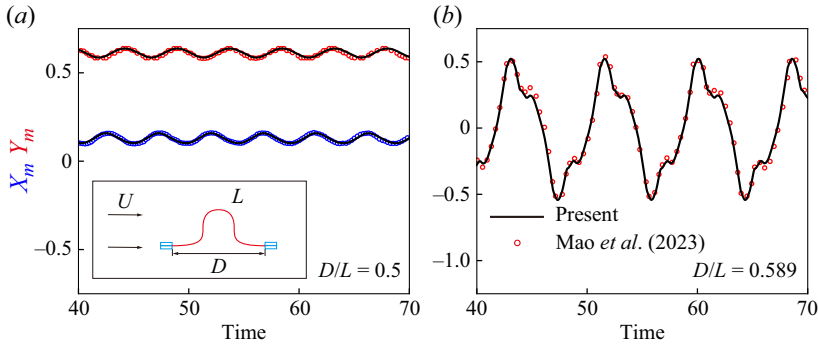


Figure 4. Position of the midpoint of the filament in the x and y directions when length ratio is equal to (a) 0.5 and (b) 0.589. The inset in figure 4(a) illustrates the simulated model including a flexible filament clamped at two edges.

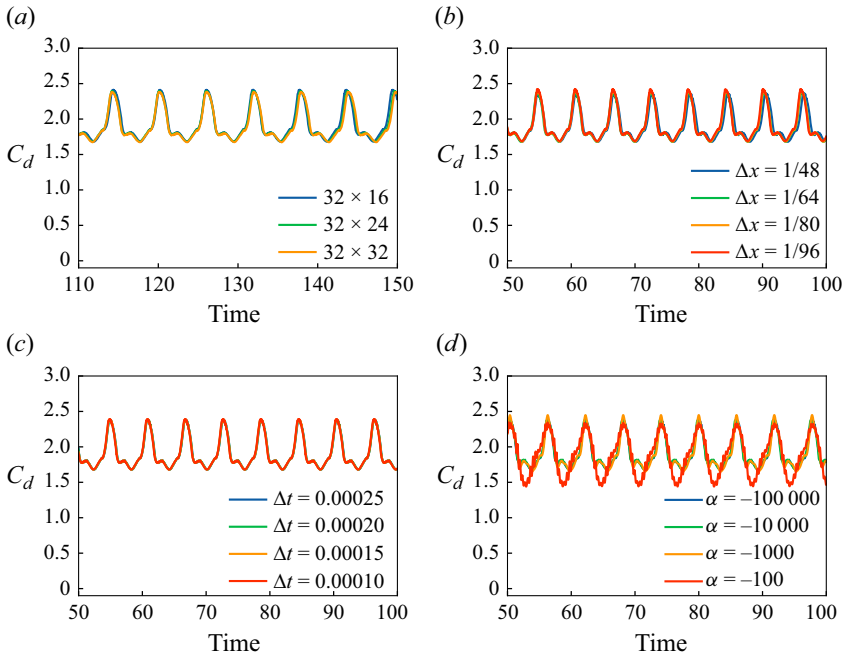


Figure 5. Impact of (a) the size of computational domain, (b) fluid mesh size Δx , (c) time step Δt and (d) free parameter α on the drag coefficient C_d .

and the value of the free coefficient α in (2.7). In these simulations, the filament length $Lr = 2.0$ and inclination angle $\theta = 45^\circ$ were fixed. Figure 5 illustrates the variation of the drag coefficient C_d over time under different parameter settings. In this study, drag is obtained by integrating the Lagrangian momentum force \mathbf{F} , and after further non-dimensionalisation, the drag coefficient C_d is obtained, where $C_d = -\int \mathbf{F}_x ds / \frac{1}{2} \rho_0 U^2 D$ with \mathbf{F}_x representing the component of \mathbf{F} in the x direction. In summary, selecting a computational domain size of 32×24 , a mesh size of $\Delta x = 1/64$, a time step of $\Delta t = 0.00025$ and a free parameter of $\alpha = -10\,000$ can ensure computational accuracy and minimise computational costs. All subsequent calculations will be performed using these parameters.

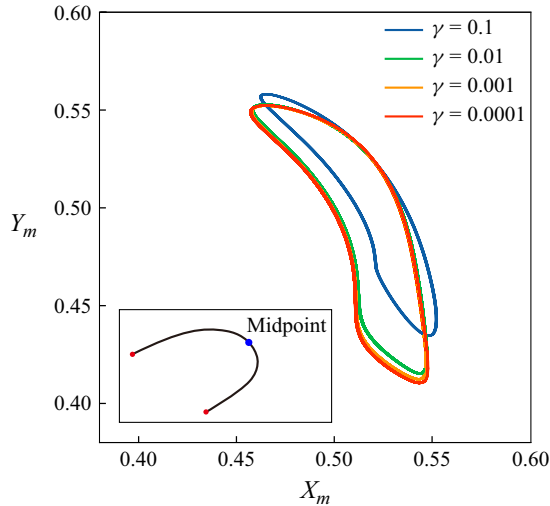


Figure 6. Impact of the bending coefficient γ on the motion trajectory of the midpoint of the filament.

Finally, the object of the study is an inextensible and sufficiently flexible filament, meaning that the bending coefficient is non-zero, but the system is not highly sensitive to changes in bending coefficient. Therefore, it is necessary to conduct a sensitivity analysis of the bending coefficient of the filament to meet the research requirements. We still simulated the motion of a filament with $Lr = 2.0$ and $\theta = 45^\circ$, conducting a bending coefficient sensitivity analysis by plotting the motion trajectories of the midpoint of the filament under different γ , as shown in figure 6. When γ exceeded 0.01, the motion trajectory was significantly affected by γ . However, when $\gamma < 0.01$, its impact was significantly reduced. Particularly, when γ was less than 0.001, the effect of γ was minimal, indicating that the filament was sufficiently flexible. Therefore, for the remaining calculations in the study, the bending coefficient was fixed at 0.001.

3. Results and discussion

3.1. Motion modes of the filament

This section investigates the motion modes and related dynamic performance of filaments under various length ratios (Lr) and inclination angles (θ). The range of Lr is set from 1.0 to 5.0 and θ spans from 0° to 90° . Notably, when $Lr = 1.0$, the filament forms a straight line and remains stationary. Therefore, if the motion equation for an inextensible filament is used for simulation, extremely small time steps are required. For this reason, this paper directly substitutes the filament in this scenario with a rigid plate for simulation. The Reynolds number Re is fixed at 100 and the bending coefficient γ is set to 0.001, as determined from the results of the previous section. Other numerical computation parameters, including the size of the computational domain, grid size and time step, are also set based on the test results presented in the previous section.

Figure 7 illustrates the distribution of filament motion modes in the θ - Lr parameter space, capturing various behaviours influenced by both filament length and inclination angle. At low θ and Lr , a rich variety of motion modes is observed, necessitating higher resolution in this region for detailed analysis. To better visualise these modes, breakpoints are added to the axes of figure 7. When $Lr = 1.0$, the filament is inextensible and equivalent to a 2-D plate. Based on whether vortex shedding occurs at different θ , the motion can be categorised into two modes: for $\theta < 30^\circ$, no vortex shedding occurs in

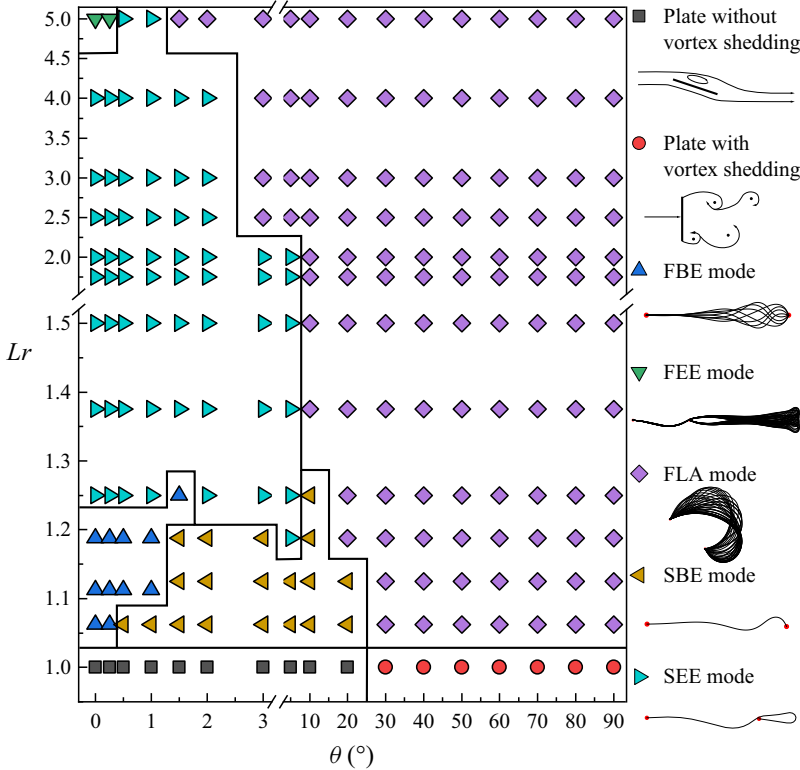


Figure 7. Distribution diagram of filament motion modes in the θ - Lr space. The FBE mode represents the filament flapping between two ends. The FEE mode represents the filament flapping and extending beyond two ends. The FLA mode represents the filament flapping at a large angle. The SBE mode represents the filament being stationary between two ends. The SEE mode represents the filament being stationary and extending beyond two ends. The right column displays the motion trajectories of the filament corresponding to different modes.

the flow field and for $\theta \geq 30^\circ$, clear vortex shedding is observed. However, when $Lr > 1.0$, the length of the filament exceeds the distance between the two fixed ends, thus allowing for the possibility of motion. Depending on whether the filament moves and the shape features of its motion, five distinct filament motion modes are identified, including three flapping modes and two stationary modes, namely, FBE (flapping between two ends), SBE (stationary between two ends), SEE (stationary and extends beyond the two ends), FEE (flapping and extending beyond the two ends) and FLA (flapping at a large angle).

As shown in figure 7, the FBE mode occurs when both θ and Lr are very small, such as $\theta < 0.25^\circ$ and $Lr \leq 1.1875$. The corresponding filament motion trajectory can be found in the right column of figure 7. Figure 8 illustrates the instantaneous shape changes of a filament in the FBE mode over one cycle, with system parameters being $\theta = 0^\circ$ and $Lr = 1.0625$. It can be observed that points along the filament do not oscillate up and down in the same phase. Instead, there exists a wave propagating along the filament in the x direction, resulting in phase differences at various positions. For instance, the lowest position in the y direction occurs near the midpoint of the filament at $t = 0$. As t increases, this lowest position continuously moves downstream, approaching the downstream fixed point by $t = T/2$. Moreover, when observing the shape of the filament near the downstream fixed point, a sudden transition in the position of the filament due to wave propagation can be found. From $t = 0$ to $t = 3T/8$, the end part of the filament

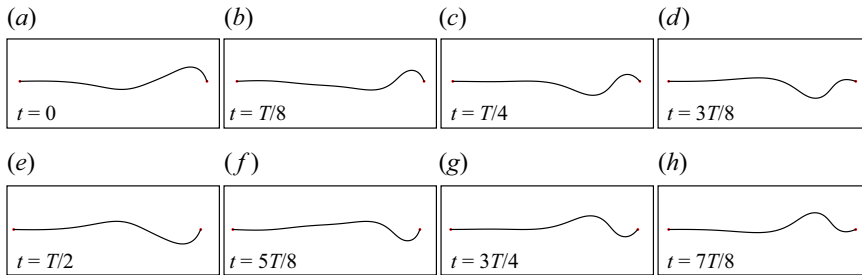


Figure 8. Shape variation of a filament in the FBE mode within one cycle, with parameters being $\theta = 0^\circ$ and $Lr = 1.0625$.

moves from its upper limit position to a middle position. However, in the shorter time span from $t = 3T/8$ to $t = T/2$, due to the propagation of the trough along the x direction, the end part of the filament abruptly shifts from the middle position to its lower limit position. This rapid change in the filament position over a short period resembles the snap-through oscillation mentioned by Mao *et al.* (2023). Furthermore, as shown in figure 7, the FBE mode only occurs within a specific parameter range, specifically when $\theta \leq 1.5^\circ$ and $Lr \leq 1.25$. Even within this θ range, the flapping of the filament weakens with an increase in θ and the flapping becomes asymmetric when $\theta \neq 0^\circ$. As either θ or Lr continues to increase, the FBE mode cannot be sustained and the filament gradually transitions into a stationary mode.

As depicted in figure 7, based on whether the filament extends beyond the downstream fixed point or not, the stationary modes are categorised into two SBE and SEE modes. When Lr remains at a relatively small and constant value while θ increases, the flapping of most filaments in the FBE mode will weaken and become stationary between two ends (SBE mode). The shape of the filament under the SBE mode is also displayed in figure 7, where $\theta = 1^\circ$ and $Lr = 1.0625$. Due to the small θ in this case, the filament accumulates near the downstream fixed end under the influence of the incoming flow, remaining in a relatively relaxed state. However, as θ increases, the influence of the incoming flow on the underside of the filament significantly strengthens. Even though the filament remains stationary between the two ends, its shape will be deformed into a ‘bow’ under the effect of the fluid.

Similarly, when θ remains at a relatively small constant value while Lr increases, the filament in the FBE mode will eventually transition into a stationary state as well. At this point, due to the relatively large Lr exhibiting redundancy, the filament becomes stationary and extends beyond the two ends (SEE mode). Figure 7 also displays the shape of the filament under SEE mode, where $\theta = 0.5^\circ$ and $Lr = 1.75$. At this point, due to the small θ , the filament will be positioned very close to the downstream fixed point and may even break off at the downstream fixed point. The extended portion will also form a narrow tail behind the downstream fixed point. As θ increases, the distance between the filament and the downstream fixed point grows due to the influence of the incoming flow. This means the opening of the downstream loop structure gradually enlarges, allowing the loop to encompass more fluid.

It is noteworthy that when the tail formed by the filament being separated at the downstream fixed point is relatively short, the filament is in the SEE mode. However, when a longer filament results in a sufficiently long tail, the filament can no longer remain stationary and will transition into a new flapping mode. In this case, the filament is flapping and extending beyond the two ends (FEE mode), as shown in figure 7. Additionally, it is observed that the FEE mode is highly sensitive to θ , occurring only when θ is very small.

In our computational space, the FEE mode appears only at $\theta < 0.5^\circ$ and is not observed in the range of $0.5^\circ \leq \theta \leq 1^\circ$.

In fact, although the four motion modes were previously described in detail, they only occupy a relatively small portion of the θ – Lr space. As can be seen from [figure 7](#), these modes occur only when $\theta \leq 20^\circ$. Instead, the filament will exhibit a more widespread flapping at a large angle (FLA mode). In this mode, flapping is directly caused by periodic vortex shedding that occurs when θ increases and exceeds a critical value. For example, when θ exceeds 30° , vortex shedding begins for a rigid plate. Thus, within this range of angles, a flexible filament with $Lr > 1$ will also experience vortex shedding, leading to flapping. Additionally, as Lr increases, the critical value of θ at which vortex shedding begins decreases. For instance, as shown in [figure 7](#), the filament with $Lr = 5$ enters the FLA mode at as small as $\theta = 2^\circ$.

3.2. Flow field under various motion modes

To investigate the flow field surrounding the filament in different motion modes, [figure 9](#) presents the instantaneous vorticity and time-averaged pressure around the filament with $Lr = 1.125$ under various θ , encompassing the FBE mode, SBE mode and FLA mode. [Figure 9\(a,c,e\)](#) respectively represent the instantaneous vorticity ω_z for $\theta = 0^\circ$, 1° and 2° . In these figures, the green lines indicate the instantaneous positions of the filament. When $\theta = 0^\circ$, the filament is in the FBE mode, oscillating up and down between the two fixed ends. Observing its motion trajectory over time shown in the inset of [figure 9\(a\)](#), the filament tends to accumulate near the downstream fixed point under the influence of the fluid. As a result, the downstream portion of the filament exhibits more significant motion compared with the upstream portion. Consequently, stable shear layers form on both sides of the upstream portion of the filament, where the formation of vortices is also observed, as indicated in [figure 9\(a\)](#). Vortices weaken as they move downstream but are reinvigorated by the flapping of the filament, particularly at points of higher curvature (Farnell *et al.* 2004), as seen in [figure 9\(a\)](#). The periodic flapping of the filament results in a variation of vorticity over time, which is reflected in the instability of the vortices in the wake. The initiation of filament flapping in the FBE mode occurs because the length of the filament exceeds the distance between the two fixed ends, leading to an asymmetric shape at the initial moment. As a result, the filament begins to flap under the corresponding asymmetric fluid forces. However, once the filament starts flapping, if $\theta = 0^\circ$, the effects of fluid forces on both sides of the filament become balanced and, as shown in [figure 9\(b\)](#), the time-averaged pressure on both sides of the filament is equal. In summary, a comparison with the traditional 1-D flag model shows that the motion of the filament in the FEE mode is just the result of adding a fixed point to the tail of a 1-D flag (Zhang *et al.* 2000; Zhu & Peskin 2002; Connell & Yue 2007; Huang *et al.* 2007). Although the motion mode of the filament remains unchanged as θ increases from 0° to 1° , with the filament still flapping between two fixed points, the change in θ results in asymmetric flapping and reduced motion amplitude, as shown in the inset of [figure 9\(c\)](#). The shape of the vortices remains largely consistent with those at $\theta = 0^\circ$, but wake vortex instability is reduced. This is attributed to the decreased amplitude of the flapping of the filament. As θ increases, the flapping of the filament continuously weakens. When θ reaches 2° , the filament enters the SBE mode and its flapping ceases. As illustrated in [figure 9\(e\)](#), in appearance, the shape of the filament appears very similar to its configuration at $\theta = 1^\circ$. However, due to the filament being stationary, no instability of vortices is observed in the wake. [Figure 9\(b,d,f\)](#) illustrates the changes in the time-averaged pressure around the filament as θ varies from 0° to 2° . It can be observed that when $\theta = 0^\circ$, the fluid forces on both sides of the filament

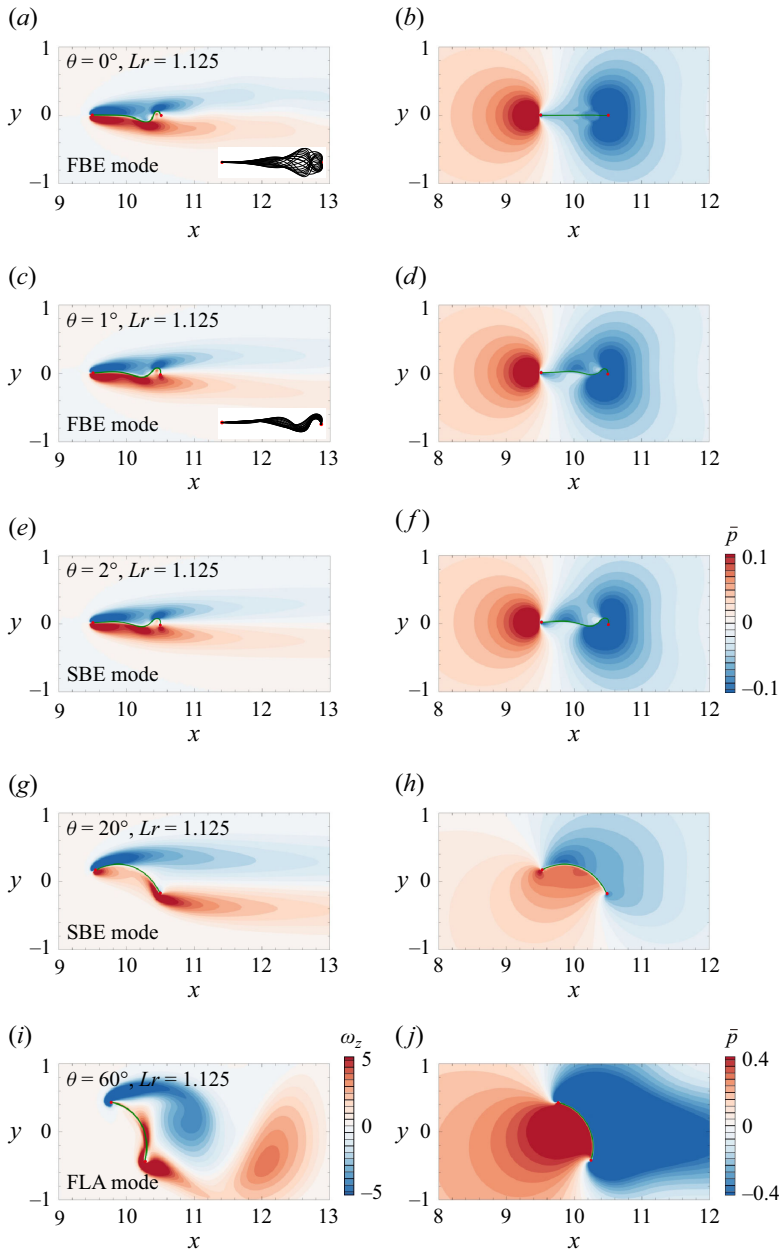


Figure 9. (a,c,e,g,i) Instantaneous vorticity and (b,d,f,h,j) time-averaged pressure of the flow field at various θ when $Lr = 1.125$. The green solid lines represent the shape of filament. The insets in figure 9(a,c) represent the motion trajectories of the filament.

have exactly the same effect, resulting in a symmetric flapping. However, when $\theta \neq 0^\circ$, the system becomes asymmetric, causing the lower side of the filament to encounter stronger fluid impacts, leading to the formation of relatively high pressure on the lower side. This high pressure suppresses the flapping of the filament, leading the filament to enter the SBE stationary mode when $\theta = 2^\circ$. It can be argued that the intrinsic asymmetry introduced by the increase in θ is the principal factor driving the transition of the motion mode from

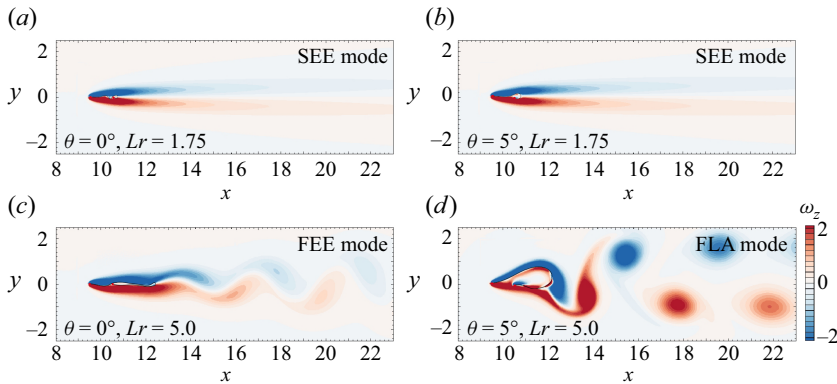


Figure 10. Instantaneous vorticity of the flow field for $Lr = 1.75$ and 5.0 under (a,c) $\theta = 0^\circ$ and (b,d) $\theta = 5^\circ$.

FBE to SBE. When θ increases from 2° to 20° , the filament remains in the SBE mode, but is subjected to more intense fluid impact, causing it to splay out into a ‘bow’ shape. Figure 9(h) show the time-averaged pressure around the filament at $\theta = 20^\circ$. Compared with figure 9(b,d,f), figure 9(h) covers a larger pressure range, hence, a different range legend is chosen to display more details of the pressure distribution. When $\theta = 20^\circ$, a significant positive pressure and negative pressure appear at the front and rear of the filament, and the ‘bow’ shape of the filament forms from the combined effects of these two pressures. This pressure distribution pattern differs from the alternating high and low pressure distribution observed when θ is smaller. In addition, when θ increases to 60° , only negative vortices are observed near the upper upstream fixed point, while only positive vortices are observed near the lower downstream fixed point, as shown in figure 9(i). This is quite different from the simultaneous appearance of positive and negative vortices near the upstream fixed point, as seen in figure 9(a,c,e,g). The vortices detach from the ends of the filament and extend downstream, with vortex shedding occurring behind the filament. The periodic vortex shedding causes variations in the external forces around the filament, inducing flapping and causing the filament to transition from the SBE mode to the FLA mode. The appearance of the Kármán vortex street is a prominent characteristic of the FLA mode, as shown in figure 9(g,i).

To further investigate the flow fields under various motion modes involved and the transition of the motion modes as Lr increases, figure 10 shows the instantaneous vorticity of the filament with $Lr = 1.75$ and 5.0 under $\theta = 0^\circ$ and 5° . This figure describes the transition from SEE mode to FEE mode or FLA mode, and the characteristics of the vorticity field under the three aforementioned modes. When $Lr = 1.75$ and $\theta = 0^\circ$, the filament is stationary, with a pair of vortices appearing on either side of the upstream filament and extending downstream. After detaching from the filament, they gradually weaken steadily and no vortex shedding occurs. Additionally, when $Lr = 1.75$, the filament extends beyond the downstream fixed point, forming a short tail. Due to $\theta = 0^\circ$, the filament itself remains close to the downstream fixed point and is separated by it. Since this short tail does not flap in the incoming flow, the entire system remains stationary. This explains why the filament, initially in the FBE mode, flapping between the two ends, transitions into the SEE stationary mode after extending beyond the downstream fixed point due to the increase in Lr . However, as Lr continues to increase and the length of the tail surpasses a threshold, the SEE mode cannot be maintained and the filament tail begins to perform periodic motion. At this point, since the filament is separated by the downstream fixed point, the motion between the two ends is very weak, while the

tail exhibits relatively larger flapping, as shown in [figure 7](#). The tail behaves similarly to a single flapping filament and the shape of the vortices also resembles that of a single filament under certain parameters (Connell & Yue 2007). For a single filament, the flapping is self-excited, where a longer filament results in an easier onset of self-induced flapping. This is consistent with the reason why the SEE mode transitions into the FEE mode as Lr increases. However, when θ increases to 5° , although the filament remains in the SEE mode, the filament with $Lr = 1.75$ captures more fluid at its tail under the influence of the incoming flow. As the filament length increases, the tail is full, which promotes vortex shedding and induces flapping, causing the filament to transition into the FLA mode, as shown in [figure 10\(b,d\)](#). Compared with the FEE mode, the FLA mode has a larger amplitude of movement, the vorticity of the wake vortex is stronger and the spacing in the y direction is larger. In summary, as seen in [figures 9 and 10](#), maintaining the stationary mode for the filament requires rather stringent parameter conditions. As θ increases, the filament can easily transition into the FLA mode due to vortex shedding. Similarly, with an increase in Lr , the filament may transition into either the FEE or FLA mode.

3.3. Analysis of the FLA mode

As can be seen from [figure 7](#), the FLA mode occupies a very large proportion of the θ - Lr space, especially when θ exceeds 30° , all filaments are in the FLA mode. Therefore, it is necessary to conduct a more detailed study on this mode.

Under the FLA mode, the flapping of the filament is caused by periodic vortex shedding behind the filament, and the flapping frequency (f) of the filament is consistent with the vortex shedding frequency. As an important parameter characterising the flapping of the filament, it is necessary to first study the changes in the flapping frequency under the FLA mode with respect to θ and Lr . The flapping frequency is determined by calculating the frequency of motion at the midpoint of the filament. This is achieved by recording the time-varying position coordinates of the midpoint of the filament in the y direction and performing a Fourier transform to obtain the frequency information. For $Lr = 1.0$, which represents a rigid plate, f is specified as the vortex shedding frequency. It should be noted that since we have non-dimensionalised all parameters prior to the numerical calculations, the frequency f we obtain is also non-dimensional, i.e. $f = f_{dim}D/U$, where f_{dim} represents the actual dimensional frequency. [Figure 11\(a\)](#) illustrates the variation of f with respect to Lr and θ , with all simulation results in the FLA mode included. Overall, f tends to decrease as both Lr and θ increase. However, when $\theta \leq 60^\circ$, the frequency difference under different θ is large, especially when θ is very small. When $\theta > 60^\circ$, the change in θ has a smaller effect on the frequency. Additionally, at larger θ , the variation range of the flapping frequency with respect to Lr becomes smaller. For instance, at $\theta = 30^\circ$, the range of flapping frequency varies from 0.125 to 0.245 under different Lr . However, at $\theta = 90^\circ$, the range of flapping frequency is between 0.115 and 0.165. Since the non-dimensionalisation process uses fixed values of D and U , the variation range of f also reflects the actual variation in dimensional frequency. Furthermore, the frequency can also be re-non-dimensionalised using a new characteristic length. Here, we use the maximum width W of the time-averaged shape of the filament. [Figure 11\(b\)](#) illustrates the definition of W , where the green line represents the time-averaged shape of the filament. [Figure 11\(c\)](#) shows the variation of W/D with Lr and θ . It can be observed that the maximum width of filament, which is vertical to the incoming flow and represented by W/D , increases monotonically with the increase of Lr and θ . The re-non-dimensionalised frequency f_w can be calculated based on W and can be derived from f , as

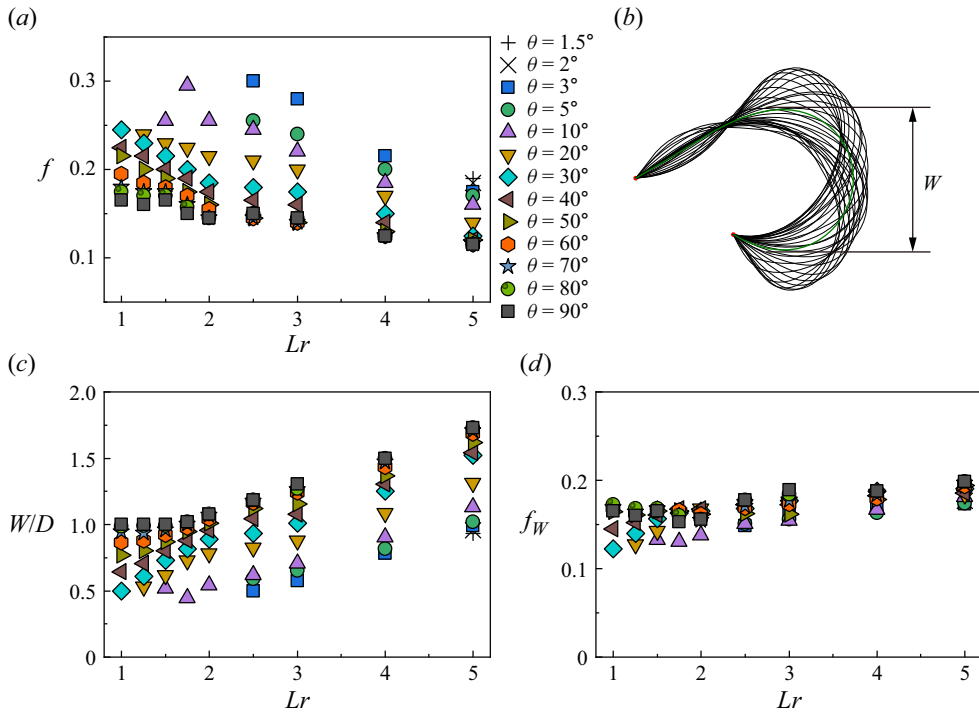


Figure 11. (a) Variation of the filament flapping frequency f with Lr and θ under the FLA mode. (b) Schematic diagram used to define the maximum width W of the time-averaged shape of the filament in the y direction. (c) Variation of W/D with Lr under various θ . (d) Variation of re-normalised frequency f_w with Lr under various θ .

$$f_w = \frac{f_{dim} W}{U} = \frac{f_{dim} D}{U} \cdot \frac{W}{D} = f \cdot \frac{W}{D}. \quad (3.1)$$

After re-normalisation, as shown in figure 11(d), the flapping frequency of the filament in the FLA mode shows little variation with respect to Lr and θ , exhibiting only a slight increase with Lr . In most cases, f_w remains approximately 0.17. This indicates that W is a fundamental parameter influencing the flapping frequency, and a larger W results in both a smaller f_{dim} and f . Therefore, based on the increasing trend of W with Lr and θ shown in figure 11(c), f decreases with increasing Lr and θ , as illustrated in figure 11(a). Finally, as observed in figure 11(d), although using W for re-normalisation yields generally good results in most cases, for $\theta \leq 10^\circ$, the re-normalised results tend to be slightly underestimated and for $Lr \leq 1.5$, there are certain θ values where the results are also slightly smaller. This suggests that using W for re-normalisation may not be entirely appropriate in these cases.

The flapping of the filament directly affects the variation in the lift of the filament, making it essential to study the lift variation curve to analyse the specific impact of filament flapping on the lift variation process in the FLA mode. Similar to C_d , the lift coefficient C_l is obtained by non-dimensionalising the lift, denoted as $C_l = -\int F_y ds / \frac{1}{2} \rho_0 U^2 D$, where F_y represents the component of the Lagrangian momentum force F in the y direction. Through the analysis of C_l and the position of the midpoint in the y direction Y_m at $\theta \geq 30^\circ$, we found two types of lift variation process. Figure 12 displays the results under two sets of parameters: $\theta = 90^\circ$, $Lr = 2.0$ and $\theta = 90^\circ$, $Lr = 4.0$, to illustrate the two types of lift variation process. First, in figure 12(a), the solid

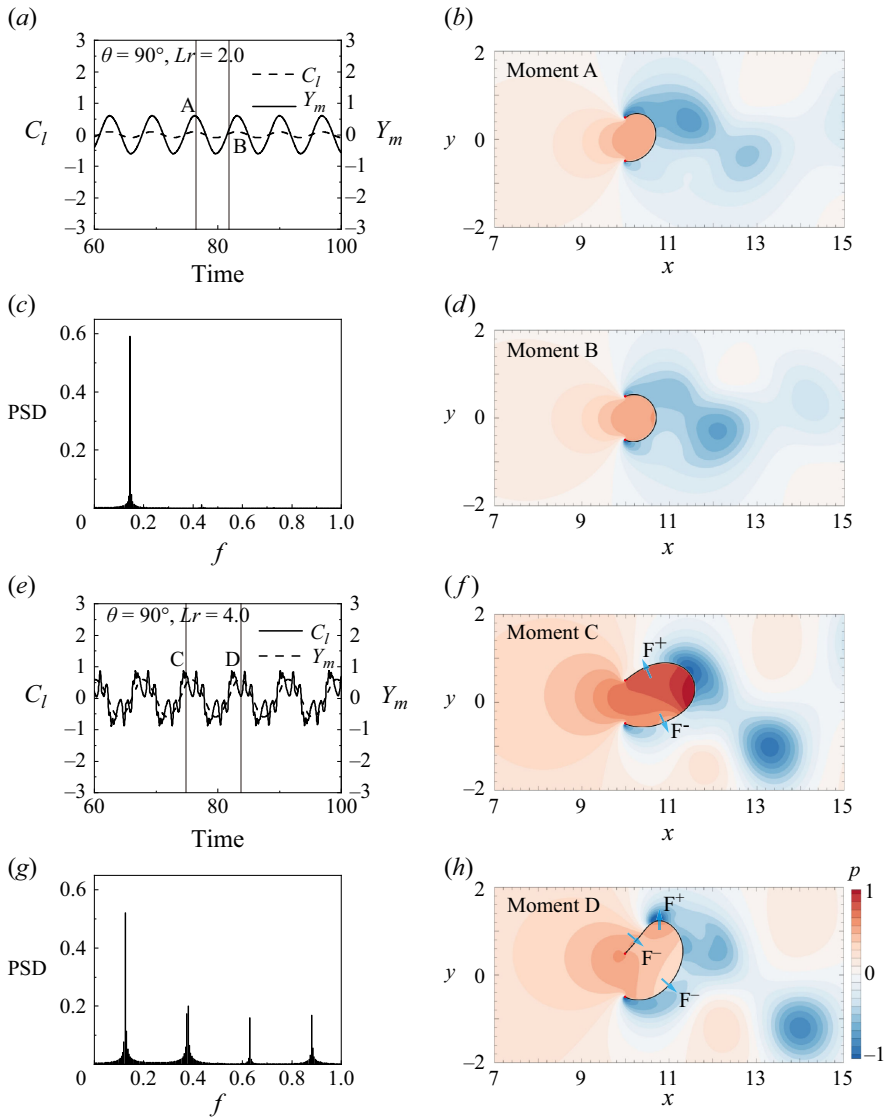


Figure 12. Lift coefficient C_l , the position of the midpoint in the y direction Y_m , the frequency spectra of C_l and the pressure distribution at the critical moment under two types of lift variation process. (a–d) First lift variation process in which C_l changes monotonically during the monotonic variation of Y_m . (e–h) Second lift variation process in which C_l fluctuates during the monotonic variation of Y_m . (b,d,f,h) Instantaneous pressure at moments A, B, C and D. The arrows represent the direction of the local forces induced by the pressure difference on either side of the filament.

line and dashed line represent C_l and Y_m changing with time, respectively. It can be seen that C_l varies periodically with time and the shape is close to a sinusoidal shape. At the same time, C_l and Y_m are in-phase. This means that as Y_m changes from its minimum value to its maximum value, the filament moves from its extreme lower position to its extreme upper position, and the lift also changes from its minimum value to its maximum value. In other words, C_l changes monotonically during the phase where Y_m changes monotonically. The spectrum obtained after the Fourier transform of C_l is shown in figure 12(c). There is only a distinct single peak at $f = 0.145$ in the frequency spectrum, which is both the

flapping frequency of the filament and the vortex shedding frequency. Figure 12(e) exhibits the other lift variation process. While C_l still changes periodically with time and has a strong correlation with the change of Y_m , the variation curve of C_l does not maintain a sinusoidal-like shape like Y_m . The maximum value of C_l does not appear at the maximum of Y_m , but appears in the process when Y_m is changing to its maximum value. When Y_m is at its maximum, the lift is at a local minimum. This indicates that, as the filament moves towards an extreme position on one side, Y_m moves monotonically to an extreme value, but C_l no longer changes monotonically and instead exhibits fluctuations. From the frequency spectra shown in figure 12(g), in addition to the frequency peak at $f = 0.125$ which corresponds to the flapping frequency and vortex shedding frequency, some other frequency peaks can also be observed. To explain the reasons for the emergence of the two types of lift variation process, the pressure distribution around the filament is shown in figure 12(b,d,f,h). Figure 12(b,d) represents the pressure distribution at two representative moments in figure 12(a), where figure 12(b) represents the moment when the filament is at its extreme position and the lift is maximum, as marked at moment A, while figure 12(d) represents the moment when the filament is at its intermediate position and the lift is close to 0, as marked at moment B. At moment A, the external pressure on the upper part is significantly lower than that on the lower part, which leads to the maximum lift of the filament as shown in figure 12(a). At moment B, the shape of the filament is nearly symmetrical. The difference in external pressure on the upper and lower parts decreases and its lift is closer to 0, which is lower than the lift at moment A. When the filament continues to move to its lower extreme position, the pressure distribution is just the opposite of that in figure 12(b) and the filament receives the maximum force in the negative y direction. The lift then changes with the flapping of the filament through this process. Similarly, in figure 12(e), we choose moments C and D to represent the moments with the maximum C_l and the maximum Y_m , respectively. At moment C, the pressure distribution around the filament is shown in figure 12(f). The pressure inside the cavity formed by the filament is higher, causing a difference in the forces on the upper and lower parts of the filament. The total force F^+ experienced by the upper part is in the positive y direction, while the total force F^- experienced by the lower part is in the negative y direction. Due to the higher pressure in the upper part of the cavity and a distinct low-pressure region behind the filament, a larger resultant force is formed in the positive y direction at moment C. At moment D, the filament is at its upper extreme position, as shown in figure 12(h). Since the filament has a broader width in the y direction at this moment, the part of the filament near the upper fixed point is directly attacked by the incoming flow, hence its external pressure is higher, thus inducing a force F^- in the negative y direction. As a result of this influence, the total lift experienced by the filament at this moment is significantly reduced compared with moment C, as shown in figure 12(e). Even though Y_m is maximum at moment D, the lift is lower than at moment C and reaches a local minimum. Therefore, the reason why the lift fluctuates rather than changes monotonically during the period of monotonically varying Y_m is that the filament undergoes complex overall shape changes due to elastic deformation during flapping. Some of these shapes, such as the elongated shape at moment C, are conducive to generating lift, while others, like the wider shape at moment D, are less favourable for lift generation.

To explore the influence of different Lr and θ on the lift variation process in the FLA mode, figure 13 further illustrates the distribution of two types of lift variation process at $\theta \geq 30^\circ$. It can be observed that $Lr = 2.5$ serves as a distinct boundary. When $Lr < 2.5$, C_l always changes monotonically during the monotonic variation of Y_m , but when $Lr > 2.5$, C_l always fluctuates during the monotonic variation of Y_m . This is because when the filament length is larger, the shape of the filament changes more complexly due

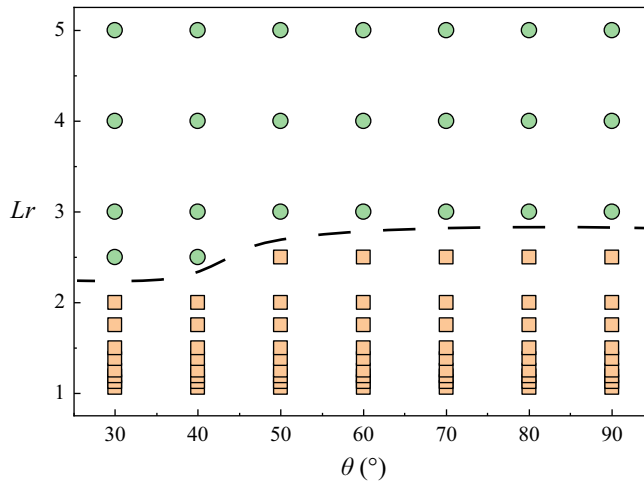


Figure 13. Distribution of two types of lift variation process under the θ - Lr space. In the first lift variation process represented by \square , C_l changes monotonically during the monotonic variation of Y_m . In the second lift variation process represented by \circ , C_l fluctuates during the monotonic variation of Y_m .

to elastic deformation during its flapping process, so the lift is more likely to fluctuate. In contrast, when the filament length is shorter, the flapping shape is uniform. Moreover, as can be seen from figure 13, θ has a slight impact on the length corresponding to the transition between two regions. At smaller θ , C_l is more likely to exhibit fluctuations. This phenomenon occurs because the cavity formed by the filament holds a smaller amount of fluid at smaller angles, resulting in a reduced degree of filling. This allows the filament greater freedom in elastic deformation, which is more conducive to the emergence of lift fluctuation.

3.4. Variation of time-averaged lift and drag

Lift and drag are critical dynamic parameters in fields such as shipbuilding, marine engineering and aerospace, with extensive research conducted on aerofoils in the aerospace sector. Studies on flexible structures have also shown that the dynamic performance of a system can be improved by locally placing flexible membranes on the aerofoil structure or by using an entire flexible membrane (Song *et al.* 2008; Waldman & Breuer 2017; Tzezana & Breuer 2019; He & Wang 2020; Mathai *et al.* 2022). Therefore, for the system in the present study, the variations in lift and drag of the flexible filament under different parameters also deserve attention.

Figure 14(a,b,c) shows the time-averaged drag coefficient $\overline{C_d}$, time-averaged lift coefficient $\overline{C_l}$ and the ratio of lift to drag $\overline{C_l}/\overline{C_d}$ under different θ and Lr , respectively. In figure 14(a), it can be found that as θ increases, the drag always increases monotonically, with the maximum drag generally occurring at $\theta = 90^\circ$. However, the change in drag with increasing Lr exhibits two distinct trends. When $\theta < 60^\circ$, the drag monotonically increases with Lr . In contrast, when $\theta > 60^\circ$, the drag initially decreases and then increases as Lr increases. This trend is clearly visible in the contour lines of figure 14(a), where the system drag for $\theta > 60^\circ$ always reaches its minimum at approximately $Lr = 2.0$. At this point, the drag experienced by the filament is significantly lower than that of a bare plate. This indicates that, within this range of angles, using a filament with a specific length in place of a flat plate can reduce drag. This unusual trend in drag variation is attributed to the specific filament causing delayed flow separation and vortex shedding,

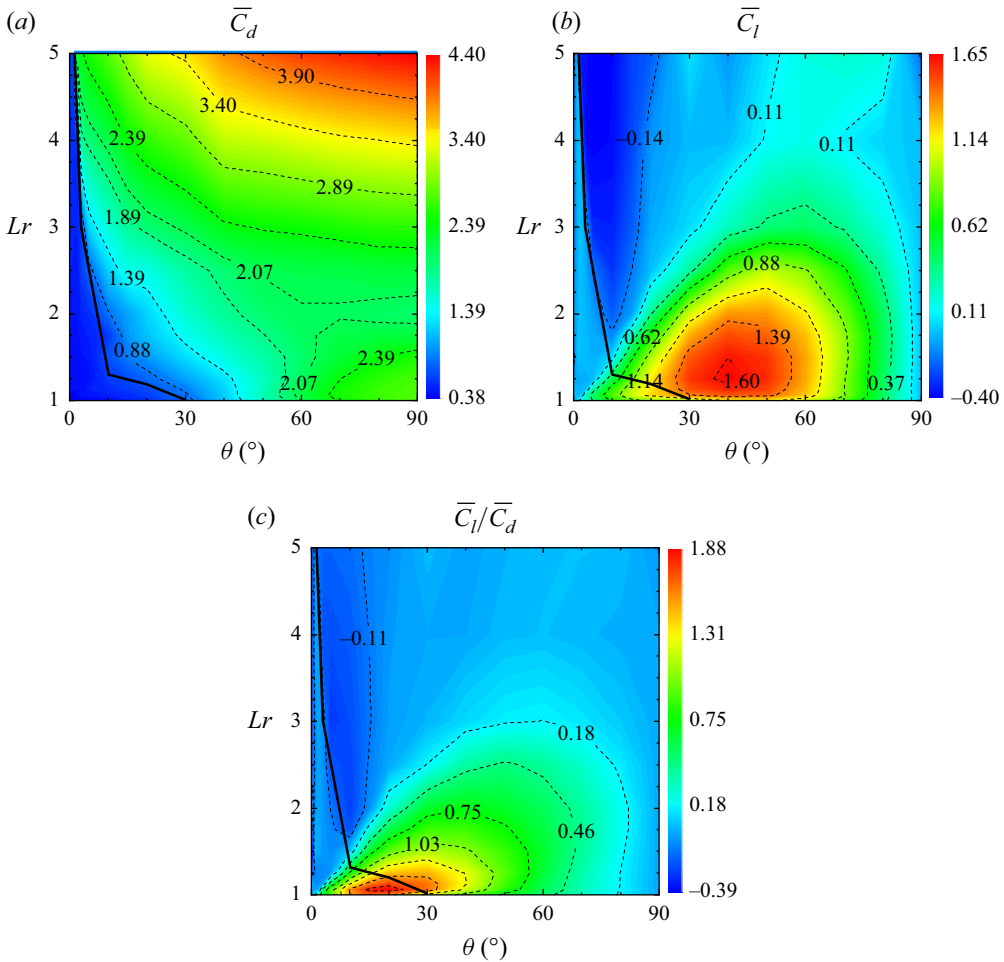


Figure 14. (a) Time-averaged drag coefficient \bar{C}_d , (b) time-averaged lift coefficient \bar{C}_l and (c) lift-to-drag ratio \bar{C}_l/\bar{C}_d under various θ and Lr . The black solid line represents the boundary between the FLA mode and other motion modes.

resulting in an increase in pressure behind the filament and, consequently, a reduction in drag, a phenomenon that has been widely studied (Mao *et al.* 2021; Sun *et al.* 2022). Considering the distribution of motion modes, it is evident that the drag in the FLA mode is significantly higher than that in other motion modes, as shown in figure 14(a), where the black solid line represents the boundary between the FLA mode and other motion modes. This is because, in the other motion modes, θ is relatively small, resulting in a weaker direct impact of the incoming flow on the filament. At this point, the frictional drag on the filament becomes more pronounced. A longer filament results in a greater frictional drag. Consequently, in figure 14(a), a slight increase in drag with Lr can be observed in these modes. Additionally, during the transition to the FLA mode, there is a significant increase in drag, especially when Lr is large. For instance, for a filament with $Lr = 5.0$, when θ increases from 1° to 1.5° , the system transitions from the SEE mode to the FLA mode, resulting in a steep increase in drag, which is visible in the upper left corner of figure 14(a). However, as Lr decreases, the magnitude of the drag increase during mode transitions decreases.

Figure 14(b) presents the contour plot of the system lift, where it is evident that the high-lift region is concentrated in the lower half of the plot. By analysing the contours, it can be observed that at $\theta = 5^\circ$, the lift of the filament with $Lr = 1.0625$ already surpasses that of the corresponding bare plate. As θ increases, the range of filament lengths capable of enhancing lift expands. In the range of $30^\circ < \theta < 60^\circ$, filaments with $Lr \leq 2.0$ can effectively enhance lift. However, when θ exceeds 70° , the contribution of the filament to lift enhancement becomes negligible. When considering filament length, it is evident that filaments with $Lr \leq 2.0$ have the potential to enhance lift. In contrast, filaments with $Lr > 2.0$ do not contribute to lift enhancement and may even result in negative lift. However, the maximum lift in the entire parameter space is observed at $Lr = 1.25$ and $\theta = 40^\circ$, representing a 45.5% increase compared with the lift of the bare plate. This indicates that although shorter filaments are generally more effective, the shortest filament is not always the best. In figure 14(b), a region including all cases of lift enhancement, specifically where $\bar{C}_l > 0.37$ is selected. Within this region, it is observed that the lift consistently increases and then decreases with increasing θ . A similar trend is also seen in the variation of lift with Lr . The phenomenon discovered in this study, where the lift of a filament with a specific length is significantly higher than that of a rigid plate, has also been observed in many studies on 3-D flexible membrane wings, with lift enhancement reaching as much as 40% (Song *et al.* 2008; He, Guo & Wang 2022). Furthermore, when considering motion modes of the filament, it can be observed that the regions of lift enhancement correspond to the SBE mode at larger θ and the FLA mode at smaller Lr . In these scenarios, the filament generally forms a bow-like shape, and either vortex shedding does not occur or, due to the smaller Lr , vortex shedding does not significantly increase the amplitude of the motion of the filament. This suggests that lift enhancement is not strongly related to vortex shedding. Instead, the primary factor is the deformation of the flexible filament in the flow field, which maintains a relatively stable ‘bow’ shape, thereby altering the surrounding pressure distribution and ultimately increasing the lift. In other motion modes, the filament does not contribute to lift enhancement.

To take into account the effects of both lift and drag, figure 14(c) shows the changes in the lift-to-drag ratio in the θ - Lr space. It can be found that the distribution of the lift-to-drag ratio closely resembles that of the lift. Within the range of $10^\circ < \theta < 60^\circ$, filaments of specific lengths have the potential to enhance the lift-to-drag ratio of the system compared with the bare plate. However, it is evident that enhancing the lift-to-drag ratio imposes stricter requirements on filament length compared with increasing lift. A significant improvement in the lift-to-drag ratio is only observed when $Lr \leq 1.5$. Longer filaments do not contribute to an improved lift-to-drag ratio. Then, the presence of the filaments can also increase the value of θ corresponding to the maximum lift-to-drag ratio. For instance, the maximum lift-to-drag ratio for the plate occurs at $\theta = 15^\circ$, whereas that for filaments with $Lr = 1.0625$ and 1.25 are 20° and 30° , respectively. Additionally, it can be observed that $Lr = 1.0625$ is an optimal length, which allows the filament to achieve the maximum lift-to-drag ratio within the range of 10° – 30° . Notably, at $\theta = 20^\circ$, this length yields the maximum value of 1.88 in the parameter space. However, for scenarios where θ exceeds 30° , a higher Lr is required to ensure the maximum lift-to-drag ratio. Based on the simulation results, $Lr = 1.0625$ and 1.125 are two suitable filament lengths that can ensure optimal outcomes within 10° – 40° . It is important to note that $Lr = 1.0625$ is the smallest filament length employed in this numerical study and this length is sufficiently small to reveal the relevant rules of lift-to-drag ratio enhancement. Similar to the lift distribution, regions with a high lift-to-drag ratio correspond to the SBE mode at larger θ and the FLA mode at smaller Lr , while the filament in other motion modes has no beneficial impact. However, the key difference is that the peak of the lift-to-drag ratio occurs in the SBE

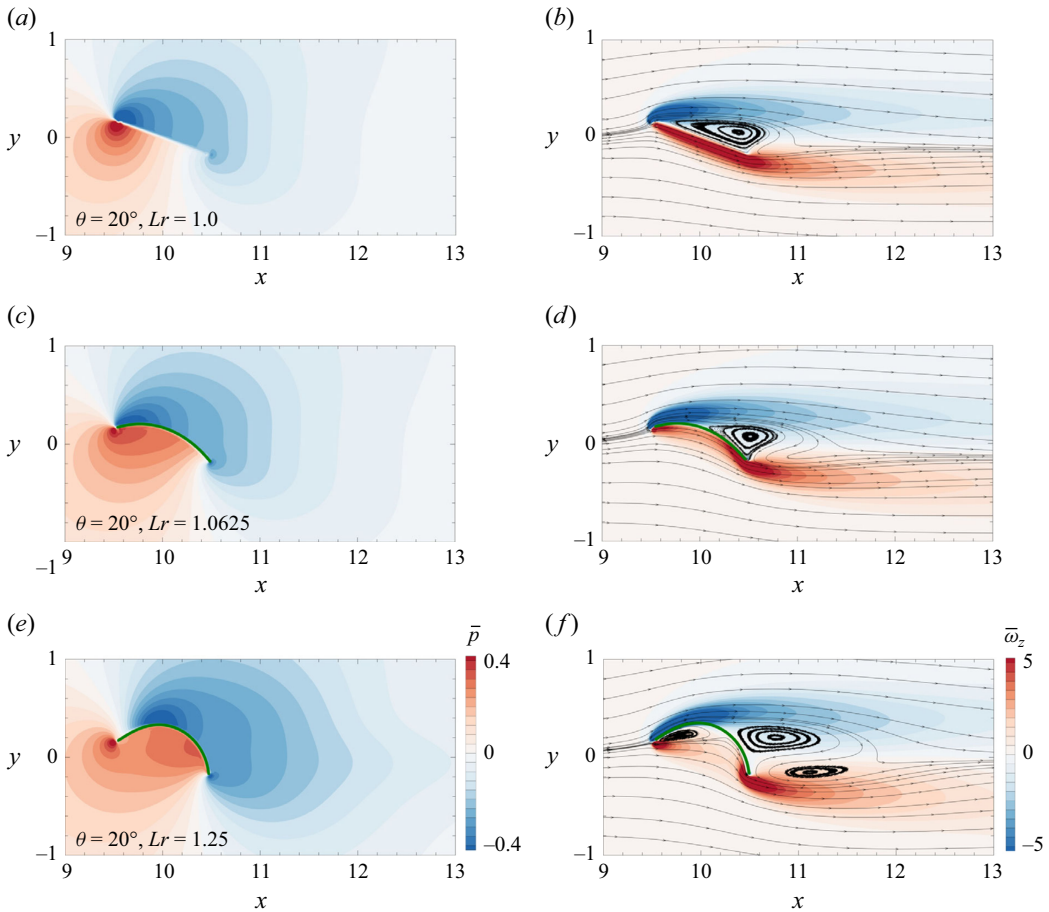


Figure 15. Time-averaged pressure, vorticity and streamlines around the filament with (a,b) $Lr = 1.0$, (c,d) 1.0625 and (e,f) 1.25 under $\theta = 20^\circ$.

mode rather than the FLA mode. This is because, although the lift is greater in the FLA mode, the drag is also significantly higher due to the larger θ . Consequently, the lift-to-drag ratio is not as high. In contrast, within the SBE mode, although the lift is relatively small, the drag is also minimal, resulting in a higher lift-to-drag ratio.

To investigate the mechanism by which short filaments increase the lift and the lift-to-drag ratio, figures 15 and 16 show the time-averaged pressure field, vorticity field and streamline distribution around the filament at $\theta = 20^\circ$ and 40° , respectively, where the lengths of the filament are $Lr = 1.0$, 1.0625 and 1.25. At $\theta = 20^\circ$ and $Lr = 1.0625$, the filament achieves the highest lift-to-drag ratio, while at $\theta = 40^\circ$ and $Lr = 1.25$, the filament achieves the maximum lift. Figure 15(a) shows the pressure distribution of the rigid plate at $\theta = 20^\circ$. Low and high pressures can be observed on the upper and lower sides of the plate, respectively. The pressure difference leads to the generation of the lift and drag on the plate. Figure 15(b) shows the corresponding vorticity field, where the black arrow lines represent the streamlines around the plate. It can be seen that the flow forks at the leading edge of the plate, with some fluid leaving the plate at the upstream fixed point, resulting in flow separation. The rest of the fluid flows along the lower side of the plate and forms strong vortices through shear, and finally leaves the plate at the downstream

fixed point. For $Lr = 1.0625$, the surrounding pressure distribution resembles that of the flat plate, as shown in [figure 15\(c\)](#). However, it is evident that under the influence of the fluid, the flexible filament forms a ‘bow’ shape and the high pressure below the filament is higher compared with that below the rigid plate, while the low pressure above the filament is lower than that above the plate. This results in a greater pressure difference between the two sides of the filament. Notably, the inclination angle is only 20° at this case, making the normal direction of points on the filament align more closely with the y direction. Consequently, the increased pressure difference has a greater impact on enhancing lift compared with drag, leading to an improved lift-to-drag ratio. However, as Lr increases to 1.25, the pressure distribution differs from that of $Lr = 1.0$ and 1.0625, with the high pressure appearing near the downstream fixed point. This is because a recirculation zone exists near the upstream fixed point, as shown in [figure 15\(e,f\)](#). The fluid does not flow along the shape of the filament from the upstream fixed point to downstream fixed point as shown in [figure 15\(b,d\)](#), but flows past the side of the recirculation zone and directly towards the filament, and then flows up or down after being obstructed by the filament, as shown in [figure 15\(f\)](#). Moreover, as seen in [figure 15\(e\)](#), the normal direction of the filament around the high-pressure area is closer to the x direction. Therefore, the effect of higher pressure on increasing the drag is larger than the lift, resulting in a lower lift-to-drag ratio at $Lr = 1.25$ compared with that at $Lr = 1.0625$.

When $\theta = 40^\circ$, the pressure difference on both sides of the filament is greater, which is the direct reason for the increase in lift of the system compared with when $\theta = 20^\circ$. The pressure distribution around the filament under different Lr is the same and the high-pressure region appears near the upstream fixed point, as shown in [figure 16\(a,c,e\)](#). Under scenarios with different Lr , the fluid uniformly bifurcates around the upstream fixed point, with a part flowing upward around the upstream fixed point of the filament and another part flowing along the filament bypassing the downstream fixed point. For $Lr = 1.25$, there is no recirculation zone on the underside of the filament, as shown in [figure 15\(f\)](#), nor a change in the high-pressure position caused by the recirculation zone. This also indicates that the presence of the recirculation zone beneath the filament only occurs when θ is relatively small. In [figure 16\(c,e\)](#), point Q is introduced to divide the filament into upper and lower parts, where the tangent direction of the filament at Q forms the same angle with the x -axis as the inclination angle. The pressure difference between both sides of the upper part of the filament, compared with the rigid plate, is increased, and its normal direction is closer to the y -axis, thereby enhancing lift. For the lower part of the filament, although its normal direction increasingly deviates from the y -axis, this adverse effect is offset by the increased pressure difference. Therefore, for the entire filament, the lift is increased, especially at $Lr = 1.25$, achieving the maximum lift within the parameter space. However, compared with $\theta = 20^\circ$, the increase in inclination angle leads to a wider width attacked by the flow, resulting in a significant increase in drag. This leads to a lower lift-to-drag ratio at $\theta = 40^\circ$. Overall, the increase in lift and the lift-to-drag ratio compared with the rigid plate is attributed to the elevated pressure difference on both sides of the filament and the deformation of the filament, which causes the normal direction of the upper part to align more closely to the lift direction.

3.5. Discussion on the motion modes

To deepen the understanding of the fixed-ends flexible filament system, this section will provide a simplified introduction to the motion behaviour of the filament. First, when not considering whether the filament is in motion or stationary, four basic filament shapes can be extracted from the computational results, as shown in [figure 17](#). Based on the relative

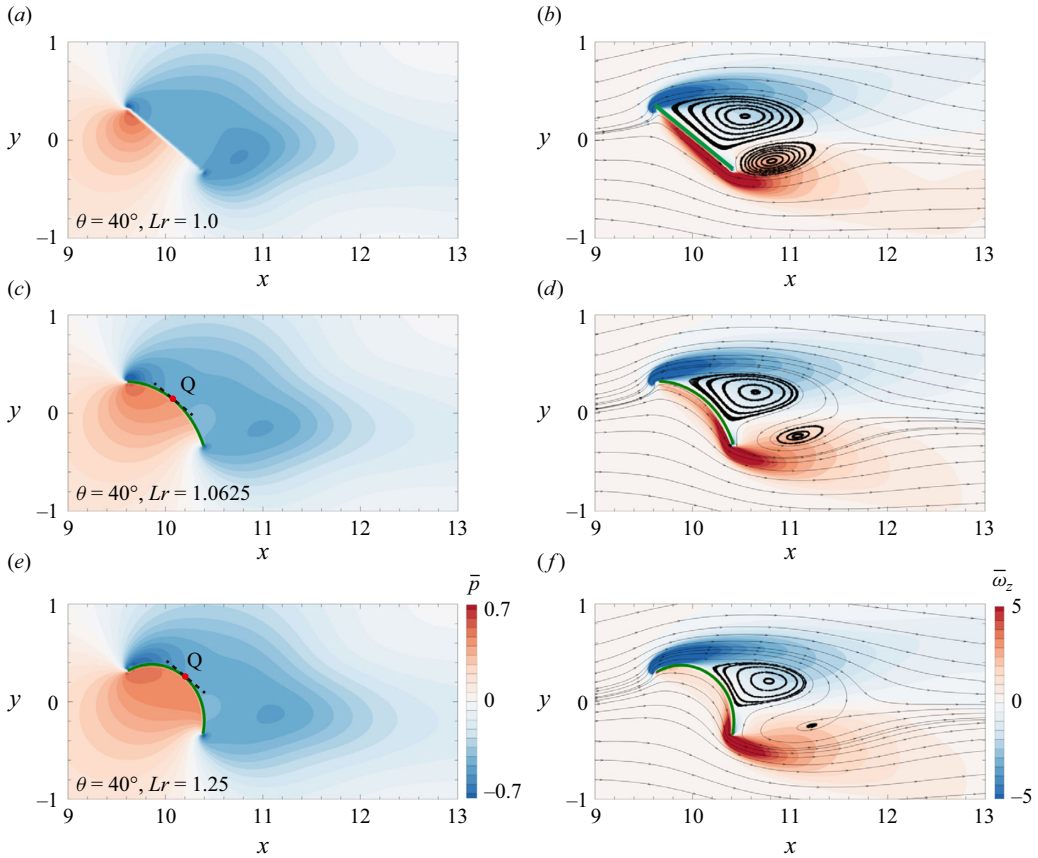


Figure 16. Time-averaged pressure, vorticity and streamlines around the filament with (a,b) $Lr = 1.0$, (c,d) 1.0625 and (e,f) 1.25 under $\theta = 40^\circ$. Point Q is introduced to divide the filament into upper and lower parts, where the tangent direction of the filament at Q forms the same angle with the x -axis as the inclination angle.

values of Lr and θ , the parameter space is divided into four regions: the $Lr_s\theta_s$ region, where both Lr and θ are relatively small; the $Lr_s\theta_l$ region, where Lr is small and θ is large; the $Lr_l\theta_s$ region, where Lr is large and θ is small; and the $Lr_l\theta_l$ region, where both Lr and θ are relatively large. In the $Lr_s\theta_s$ region, due to the small values of both Lr and θ , the filament curls near the downstream fixed point under the influence of the fluid. In the $Lr_s\theta_l$ region, the filament forms a ‘bow’ shape under the influence of stronger incoming flow force. In the $Lr_l\theta_s$ region, the filament extends beyond the downstream fixed point and, due to the smaller θ , it forms a narrow loop behind the downstream end. In the $Lr_l\theta_l$ region, the tail of the filament opens wider under the influence of the flow and wraps around more fluid. It should be noted that figure 17 is merely a schematic diagram and the boundaries between different regions in the figure are, in fact, not simple straight lines.

The four basic filament shapes described in figure 17 are intuitive and can even be summarised purely through imagination without the need for numerical simulations. However, further analysis reveals that each region contains both a stationary part and a flapping part. In the $Lr_s\theta_s$ region, when θ is very small, the filament undergoes flapping between the two fixed ends. As θ increases, the stronger fluid forces below the filament suppress the flapping, transitioning the filament into a stationary state. In the $Lr_s\theta_l$ region,

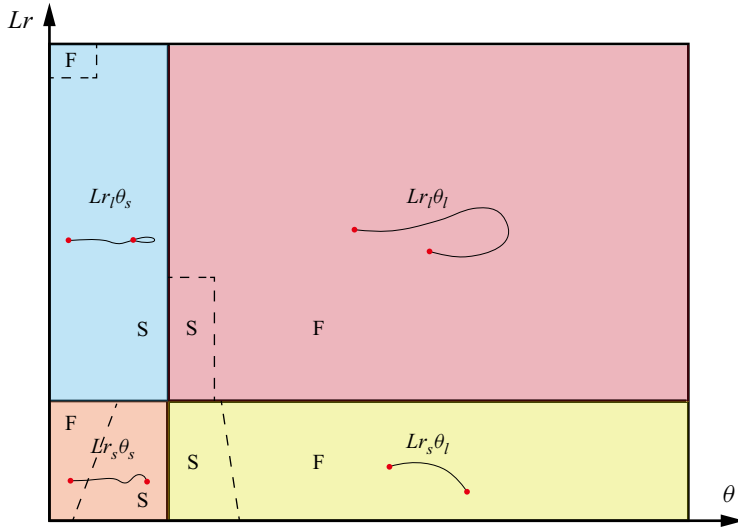


Figure 17. Schematic diagram of the distribution of the shapes of filaments in the θ - Lr space. Based on the relative values of Lr and θ , the parameter space is divided into four regions: the $Lr_s\theta_s$ region, where both Lr and θ are relatively small; the $Lr_s\theta_l$ region, where Lr is small and θ is large; the $Lr_l\theta_s$ region, where Lr is large and θ is small; and the $Lr_l\theta_l$ region, where both Lr and θ are relatively large. The four filament shapes reflect the characteristics of their respective regions. Moreover, each region consists of two parts: a stationary (S) part and a flapping (F) part.

the presence or absence of vortex shedding, primarily controlled by θ , determines the boundary between the stationary parts and the flapping part, which is similarly the case in the $Lr_l\theta_l$ region. In the $Lr_l\theta_s$ region, the filament length is the dominant factor in separating the stationary and flapping parts. A larger Lr leads to a more extended narrow tail downstream, which eventually becomes unstable and begins to flap. In summary, compared with figure 7, the flapping part in the $Lr_s\theta_s$ region corresponds exactly to the FBE mode. The stationary parts in the $Lr_s\theta_s$ region and $Lr_s\theta_l$ region both belong to the SBE mode. The stationary parts in the $Lr_l\theta_s$ region and $Lr_l\theta_l$ region belong to the SEE mode. The flapping part in the $Lr_l\theta_s$ region matches the FEE mode, and the flapping parts in the $Lr_s\theta_l$ region and $Lr_l\theta_l$ belong to the FLA mode.

3.6. Effect of γ on the motion modes

In § 2, the variations in the motion trajectories of the midpoint of the filament under different bending coefficients were investigated. It was observed that when $\gamma < 0.01$, the changes in γ had minimal impact on the motion of the filament. As a result, a fixed value of $\gamma = 0.001$ was chosen to conduct the main study, disregarding the influence of γ . Although the primary focus of our study is on the very soft filament and a carefully chosen value of γ was determined through a reasonable approach, it is undeniable that γ , as an important parameter of the filament, will impact the motion modes of the system. Thus, based on the results shown in figure 6, the filament with a larger bending coefficient of $\gamma = 0.1$ is selected for further investigation to evaluate the impact of bending coefficient.

Figure 18 illustrates the motion mode distribution of filament in the θ - Lr space for $\gamma = 0.1$. Compared with $\gamma = 0.001$, the motion mode distribution of filament under a higher γ exhibits only two main differences. First, the FBE mode does not occur at very small Lr , but instead emerges at larger Lr . For instance, at $\gamma = 0.001$, a filament with $Lr = 1.0625$ and $\theta = 0^\circ$ flaps between two fixed ends. However, under $\gamma = 0.1$, a filament

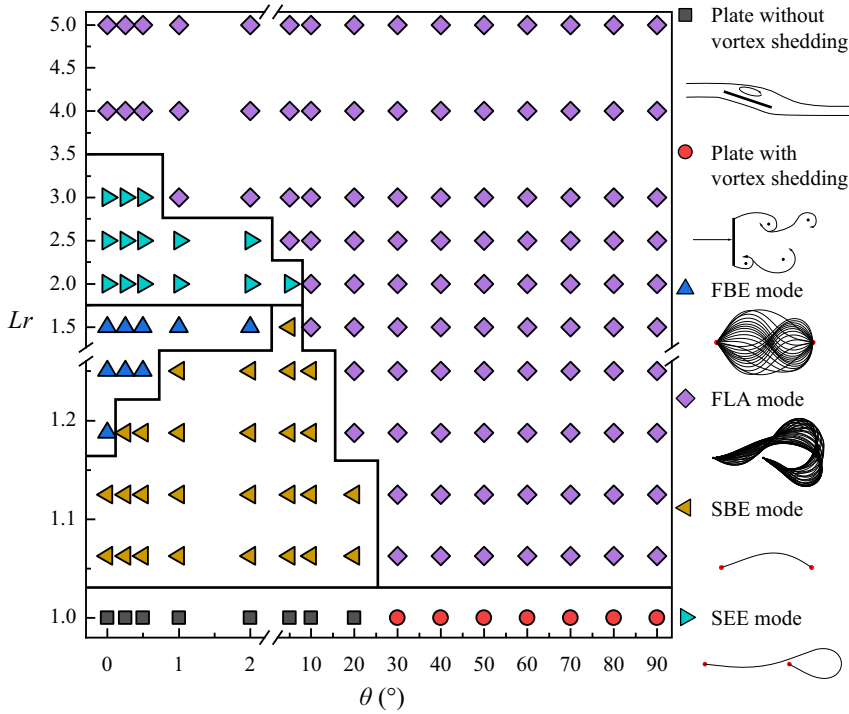


Figure 18. Distribution diagram of filament motion modes in the θ - Lr space at $\gamma = 0.1$.

with the same Lr and θ remains in a stationary state, as shown in the lower left corner of figure 18 under the SBE mode. This is because the increased bending coefficient makes the filament stiffer, allowing it to resist unbalanced fluid forces and maintain a stationary state. As the filament length increases, the imbalance of fluid forces on both sides of the filament becomes more pronounced, preventing the filament from maintaining a stationary state and resulting in flapping motion. As shown in figure 18, the filament enters the FBE mode only when its length increases to $Lr = 1.1875$ at $\theta = 0^\circ$. Second, the region of the FLA mode expands to scenarios with smaller θ , especially when Lr is relatively large. For example, at $\gamma = 0.001$, a filament with $\theta = 1^\circ$ and $Lr = 5.0$ is in the SEE mode, where the filament extends from the downstream fixed end, with its tail remaining narrow in the y direction and in a stationary state. However, at $\gamma = 0.1$, due to the higher bending coefficient, the filament with the same θ and Lr cannot undergo large-curvature deformation to maintain a narrow tail. Instead, the tail exhibits a greater width in the y direction, which promotes vortex shedding and causes the filament to flap, transitioning into the FLA mode.

4. Conclusions

This paper investigated the dynamic performance of a flexible filament fixed at both ends at different inclination angles θ . The immersed boundary method (IBM) was used to solve the interaction between the fluid and the structure. A set of parameters was obtained to guarantee computational accuracy through independent analyses of the computational domain size, fluid grid size, computational time step and the free coefficient in the IBM. By testing the effects of different bending coefficients on filament motion, a sufficiently small bending coefficient $\gamma = 0.001$ was chosen to preserve the authenticity of the filament and reduce the influence of bending forces.

First, the motion of the filament in the θ - Lr space was divided into three flapping modes and two stationary modes according to its shape features, and a detailed introduction was given to the shape features and the distribution in the θ - Lr space of different modes. The flow field characteristics of different motion modes and the mode transition were analysed by showing the pressure field and the vorticity field of different motion modes. Second, since the FLA mode occupied a very large proportion in the θ - Lr space, a more in-depth study of this mode was conducted. The results showed that the dimensionless flapping frequency f based on the distance D between two fixed ends, generally decreased with the increase of Lr and θ , whereas the dimensionless flapping frequency f_W , non-dimensionalised by the maximum width W of the time-averaged shape of the filament, showed little variation with the change in Lr and θ . This indicated that W was an important parameter influencing the flapping frequency of the filament, and the effects of Lr and θ on the flapping frequency were related to their impact on W . In addition, under this mode, two types of lift variation process were observed. More specifically, as the filament moved in a certain direction, with Y_m changing monotonically, C_l exhibited either a monotonic change or fluctuations. The fluctuations in C_l were further attributed to the effects of various shapes resulting from the elastic deformation of the filament. By studying the distribution of these two types of lift variation process in the θ - Lr space, it was found that $Lr = 2.5$ was a boundary. Longer filaments, due to their greater degrees of freedom in shape variation, were more likely to exhibit lift fluctuations. Lastly, an in-depth study of the total lift, drag and lift-to-drag ratio of the system was conducted. The drag rose with the increase in θ , with the maximum drag occurring at $\theta = 90^\circ$. Here, $\theta = 60^\circ$ was a critical angle. The drag increased with the increase of Lr at $\theta < 60^\circ$, but at $\theta > 60^\circ$, the minimum drag always occurred at $Lr = 2.0$, which suggests that a filament of a specific length can reduce drag compared with a rigid plate. Overall, the drag in the FLA mode is significantly higher than that in other motion modes. As for lift, only at $Lr \leq 2.0$ would the filament produce greater lift than the plate. The largest lift was obtained at $\theta = 40^\circ$ and $Lr = 1.25$, which was approximately a 45.5% increase compared with the rigid plate. The improvement in the lift-to-drag ratio imposes stricter requirements on the filament length, with filaments at $Lr \leq 1.5$ having a non-negligible effect on enhancing the lift-to-drag ratio. By judging from the computational results, filaments with $Lr = 1.0625$ and $Lr = 1.125$ could distinctly enhance the filament lift-to-drag ratio within a large θ range. Considering the motion modes of the filament, the regions with higher lift and lift-to-drag ratios often correspond to the SBE mode with a larger θ or the FLA mode with a smaller Lr , where the filament exhibits a 'bow' shape. Upon performing flow field analysis, it can be concluded that the main reasons for the increase in lift are the increase in pressure difference on both sides of the filament and the upper part of the flexible filament having a normal direction closer to the y direction. Coupled with the fact that the drag on the filament with small Lr did not significantly increase compared with a flat plate, this ultimately led to a greater lift-to-drag ratio.

This paper uses an in-house fluid-structure interaction solver to study the motion of flexible filaments in two-dimensional flow under different θ , providing a deeper understanding of this system. However, there are still some limitations to this research. First, the 1-D flexible filament studied in this paper is a simplification of a membrane with infinite span in a 3-D flow field, which still differs from a real-world full 3-D models with finite span. For the model with finite span, the flow along the spanwise direction as well as the overall flapping along the span and local 3-D bending need to be considered. These factors contribute to a more complex motion modes of the system. To give the simplest example, when θ is large enough to cause vortex shedding, the model with finite span requires attention not only to vortex shedding at the fixed leading and trailing edges, but

also to vortex shedding at the spanwise edges. In this case, the span length itself has a significant impact on vortex shedding and the final motion of the membrane. Second, due to the constraints of the developed solver, this paper can only examine laminar flow at low Reynolds numbers, which differs from the high-Reynolds-number turbulent problems faced in actual engineering. Therefore, our future work will focus on developing of a full 3-D high-Reynolds-number solver and conducting wider research on related problems.

Acknowledgement. The authors would like to thank the Center for High Performance Computing, Shanghai Jiao Tong University, for their support.

Funding. This work is supported by the National Key Research and Development Plan (Grant No. 2023YFC3107404) and National Natural Science Foundation of China (Grant No. 52422110).

Data availability. The data that support the findings of this study are available within the article.

Declaration of interests. The authors report no conflict of interest.

REFERENCES

- ALBEN, S., SHELLEY, M. & ZHANG, J. 2002 Drag reduction through self-similar bending of a flexible body. *Nature* **420** (6915), 479–481.
- ALBEN, S. & SHELLEY, M.J. 2008 Flapping states of a flag in an inviscid fluid: bistability and the transition to chaos. *Phys. Rev. Lett.* **100** (7), 074301.
- BAGHERI, S., MAZZINO, A. & BOTTARO, A. 2012 Spontaneous symmetry breaking of a hinged flapping filament generates lift. *Phys. Rev. Lett.* **109** (15), 154502.
- BAI, Q., LIAO, X.-W., CHEN, Z.-W., GAN, C.-Z., ZOU, H.-X., WEI, K.-X., GU, Z. & ZHENG, X.-J. 2022 Snap-through triboelectric nanogenerator with magnetic coupling buckled bistable mechanism for harvesting rotational energy. *Nano Energy* **96**, 107118.
- CONNELL, B.S. & YUE, D.K. 2007 Flapping dynamics of a flag in a uniform stream. *J. Fluid Mech.* **581**, 33–67.
- FARNELL, D.J., DAVID, T. & BARTON, D. 2004 Numerical simulations of a filament in a flowing soap film. *Intl J. Numer. Meth. Fluids* **44** (3), 313–330.
- GOLDSTEIN, D., HANDLER, R. & SIROVICH, L. 1993 Modeling a no-slip flow boundary with an external force field. *J. Comput. Phys.* **105** (2), 354–366.
- GOSELIN, F., DE LANGRE, E. & MACHADO-ALMEIDA, B.A. 2010 Drag reduction of flexible plates by reconfiguration. *J. Fluid Mech.* **650**, 319–341.
- GURUGUBELLI, P.S. & JAIMAN, R.K. 2015 Self-induced flapping dynamics of a flexible inverted foil in a uniform flow. *J. Fluid Mech.* **781**, 657–694.
- HE, X., GUO, Q. & WANG, J. 2022 Regularities between kinematic and aerodynamic characteristics of flexible membrane wing. *Chin. J. Aeronaut.* **35** (11), 209–218.
- HE, X. & WANG, J.-J. 2020 Fluid–structure interaction of a flexible membrane wing at a fixed angle of attack. *Phys. Fluids* **32** (12), 127102.
- HUANG, W.-X., SHIN, S.J. & SUNG, H.J. 2007 simulation of flexible filaments in a uniform flow by the immersed boundary method. *J. Comput. Phys.* **226** (2), 2206–2228.
- HUANG, W.-X. & SUNG, H.J. 2009 An immersed boundary method for fluid–flexible structure interaction. *Comput. Meth. Appl. Mech. Engng* **198** (33–36), 2650–2661.
- HUBER, G. 2000 Swimming in flatsea. *Nature* **408** (6814), 777–778.
- KIM, D., COSSÉ, J., CERDEIRA, C.H. & GHARIB, M. 2013 Flapping dynamics of an inverted flag. *J. Fluid Mech.* **736**, R1.
- KIM, H., LAHOOTI, M., KIM, J. & KIM, D. 2021 Flow-induced periodic snap-through dynamics. *J. Fluid Mech.* **913**, A52.
- KIM, H., ZHOU, Q., KIM, D. & OH, I.-K. 2020 Flow-induced snap-through triboelectric nanogenerator. *Nano Energy* **68**, 104379.
- MAO, Q., LIU, Y. & SUNG, H.J. 2023 Snap-through dynamics of a buckled flexible filament in a uniform flow. *J. Fluid Mech.* **969**, A33.
- MAO, Q., ZHAO, J., LIU, Y. & SUNG, H.J. 2021 Drag reduction by a flexible afterbody. *Phys. Fluids* **33** (12), 122009.
- MAO, Q., ZHAO, J., LIU, Y. & SUNG, H.J. 2022 Drag reduction by a flexible hairy coating. *J. Fluid Mech.* **946**, A5.

- MATHAI, V., TZEZANA, G.A., DAS, A. & BREUER, K.S. 2022 Fluid–structure interactions of energy-harvesting membrane hydrofoils. *J. Fluid Mech.* **942**, R4.
- MAZHARMANESH, S., YOUNG, J., TIAN, F.-B., RAVI, S. & LAI, J.C. 2022 Energy harvesting of inverted piezoelectric flags in an oscillating flow. *J. Fluid. Struct.* **115**, 103762.
- MICHELIN, S. & DOARÉ, O. 2013 Energy harvesting efficiency of piezoelectric flags in axial flows. *J. Fluid Mech.* **714**, 489–504.
- MICHELIN, S., SMITH, S.G. & GLOVER, B.J. 2008 Vortex shedding model of a flapping flag. *J. Fluid Mech.* **617**, 1–10.
- MÜLLER, U.K. 2003 Fish'n flag. *Science* **302** (5650), 1511–1512.
- ORREGO, S., SHOELE, K., RUAS, A., DORAN, K., CAGGIANO, B., MITTAL, R. & KANG, S.H. 2017 Harvesting ambient wind energy with an inverted piezoelectric flag. *Appl. Energy*. **194**, 212–222.
- PESKIN, C.S. 2002 The immersed boundary method. *Acta Numer.* **11**, 479–517.
- SADER, J.E., COSSÉ, J., KIM, D., FAN, B. & GHARIB, M. 2016 Large-amplitude flapping of an inverted flag in a uniform steady flow—a vortex-induced vibration. *J. Fluid Mech.* **793**, 524–555.
- SONG, A., TIAN, X., ISRAELI, E., GALVAO, R., BISHOP, K., SWARTZ, S. & BREUER, K. 2008 Aeromechanics of membrane wings with implications for animal flight. *AIAA J.* **46** (8), 2096–2106.
- SUN, Y., PENG, Z.-R., YANG, D., XIONG, Y., WANG, L. & WANG, L. 2022 Dynamics of a rigid-flexible coupling system in a uniform flow. *J. Fluid Mech.* **943**, A44.
- TANG, L., PAÏDOUSSIS, M.P. & JIANG, J. 2009 Cantilevered flexible plates in axial flow: energy transfer and the concept of flutter-mill. *J. Sound Vib.* **326** (1-2), 263–276.
- TRIANTAFYLLOU, M.S., TRIANTAFYLLOU, G. & YUE, D. 2000 Hydrodynamics of fishlike swimming. *Annu. Rev. Fluid Mech.* **32** (1), 33–53.
- TZEZANA, G.A. & BREUER, K.S. 2019 Thrust, drag and wake structure in flapping compliant membrane wings. *J. Fluid Mech.* **862**, 871–888.
- UHLMANN, M. 2005 An immersed boundary method with direct forcing for the simulation of particulate flows. *J. Comput. Phys.* **209** (2), 448–476.
- WALDMAN, R.M. & BREUER, K.S. 2017 Camber and aerodynamic performance of compliant membrane wings. *J. Fluid. Struct.* **68**, 390–402.
- YE, H., WEI, H., HUANG, H. & LU, X.-Y. 2017 Two tandem flexible loops in a viscous flow. *Phys. Fluids* **29** (2), 021902.
- YU, Y., LIU, Y. & CHEN, Y. 2017 Vortex dynamics behind a self-oscillating inverted flag placed in a channel flow: time-resolved particle image velocimetry measurements. *Phys. Fluids* **29** (12), 125104.
- YU, Z. 2005 A dlm/fd method for fluid/flexible-body interactions. *J. Comput. Phys.* **207** (1), 1–27.
- ZHANG, J., CHILDRESS, S., LIBCHABER, A. & SHElLEY, M. 2000 Flexible filaments in a flowing soap film as a model for one-dimensional flags in a two-dimensional wind. *Nature* **408** (6814), 835–839.
- ZHANG, X., HE, G. & ZHANG, X. 2020 Fluid–structure interactions of single and dual wall-mounted 2d flexible filaments in a laminar boundary layer. *J. Fluid. Struct.* **92**, 102787.
- ZHU, L. & PESKIN, C.S. 2002 Simulation of a flapping flexible filament in a flowing soap film by the immersed boundary method. *J. Comput. Phys.* **179** (2), 452–468.